

## Article

# Fabrication of Nanoparticle Agglomerate Films by Spark Ablation and Their Application in Surface-Enhanced Raman Spectroscopy

Petra Pál<sup>1</sup>, Viktória Horváth<sup>2</sup>, Laura Juhász<sup>3</sup> , Zoltán Kóródi<sup>1</sup>, Attila Kohut<sup>2,\*</sup> and Istvan Csarnovics<sup>1</sup> 

<sup>1</sup> Department of Experimental Physics, Institute of Physics, Faculty of Science and Technology, University of Debrecen, 4032 Debrecen, Hungary

<sup>2</sup> Department of Optics and Quantum Electronics, University of Szeged, 6720 Szeged, Hungary

<sup>3</sup> Department of Solid State Physics, Institute of Physics, Faculty of Science and Technology, University of Debrecen, 4032 Debrecen, Hungary

\* Correspondence: kohut.attila@szte.hu

**Abstract:** This paper presents a systematic study of the investigation of nanoparticle (NP) agglomerate films fabricated via depositing spark-generated Au, Ag, and Au/Ag NPs onto quartz microscope coverslips in a low-pressure inertial impactor. The primary focus of the study is to characterize these nanostructures and to examine their potential application in surface-enhanced Raman spectroscopy (SERS). The characterization of the produced nanostructures was carried out by performing optical absorbance measurements, morphology, and composition analysis, as well as testing the SERS performance of the NP films at three different excitation laser wavelengths in the visible range. The study aims to investigate the relationship between the optical properties, the morphology, and the enhancement of the produced samples at different excitations, and the results are presented and discussed. The study highlights the potential of using spark ablation and inertial impaction-based deposition as a method for producing nanoparticle films for SERS.



**Citation:** Pál, P.; Horváth, V.; Juhász, L.; Kóródi, Z.; Kohut, A.; Csarnovics, I. Fabrication of Nanoparticle Agglomerate Films by Spark Ablation and Their Application in Surface-Enhanced Raman Spectroscopy. *Chemosensors* **2023**, *11*, 180. <https://doi.org/10.3390/chemosensors11030180>

Academic Editors: Shan Cong and Chunlan Ma

Received: 1 February 2023

Revised: 27 February 2023

Accepted: 3 March 2023

Published: 7 March 2023



**Copyright:** © 2023 by the authors. Licensee MDPI, Basel, Switzerland. This article is an open access article distributed under the terms and conditions of the Creative Commons Attribution (CC BY) license (<https://creativecommons.org/licenses/by/4.0/>).

**Keywords:** nanoparticle films; spark ablation; Au/Ag alloy; surface roughness; SERS

## 1. Introduction

Nanostructured films fabricated via the deposition of nanoparticle (NP) agglomerates onto a substrate are usually characterized by relatively high porosity, i.e., a considerable ratio of the empty-to-total volume of the film. Such structures exhibit a high surface-to-volume ratio, which makes them desirable in applications, such as catalysis [1,2], gas sensing [3,4], or surface-enhanced Raman spectroscopy (SERS) [5–7], just to mention a few. There are many ways to produce and deposit NPs, among which we will focus on the so-called aerosol techniques, which result in the formation of particles dispersed in a gaseous medium [8,9]. Aerosol-based NP generation methods can be combined with direct deposition methods, such as collection on filters [10], impaction printing [11,12], thermophoretic- [3,13], or electric field-guided deposition [14,15], hence providing powerful tools to fabricate nanoparticle films for various applications.

One aerosol technique, which offers exceptionally high flexibility in terms of the NPs' material is based on the vaporization of bulk electrodes by energetic spark discharges. This method often called spark ablation only requires a controlled, atmospheric-pressure gaseous environment and a pair of electrically conductive electrodes, between which a transient spark plasma creates a vapor plume from the electrodes' material, which will condense into nanoparticles [16]. By varying the electrical properties of the discharge [17–22], the geometry of the electrodes and the surrounding chamber [23–26], the properties of the electrode material [27–30], or the properties of the carrier gas [31–33], one can tune the characteristics of the generated particles. Since spark ablation can conveniently be used to produce multielement NPs by simply combining dissimilar alloyed or

compacted electrodes [34,35], this tunability even includes the crystal structure of the produced particles [29,36,37]. NPs generated via spark ablation have been successfully used in various applications, such as gas- [4,38–43] and light [44] sensors, catalytic surfaces [45,46], or SERS substrates [10,12,47–50]. These applications used different approaches to deposit the NPs to a surface, starting from the most straightforward filtering [10] to a highly sophisticated, electrical field-assisted 3D microprinting method [49]. Among all the different approaches, the impaction-based deposition has already been shown to be sufficiently simple to integrate into an industrial-level NP printer [11,45] and versatile enough to be applicable on various substrates, including optical fibers [50] or polymers [51].

In this work, we present a systematic study on the investigation of NP agglomerate films, fabricated via depositing spark-generated Au/Ag binary NPs onto quartz microscope coverslips in a low-pressure inertial impactor. The characterization of the produced nanostructures was carried out having SERS as the main potential application in mind because it is a powerful analytical technique with broad usability in fields like biomedical analysis, environmental monitoring, and security, to mention but a few [52]. Since SERS is based on the enhancement of the Raman signal of an analyte due to the localized surface plasmon—which is the collective oscillation of electrons—resonance (LSPR) in an appropriate nanostructure, the fabrication and understanding of the relationship between the properties of such structures and their enhancement properties are of great importance. Here, pure Au, Ag, and Au/Ag alloys were chosen as a materials system, due to their well-known advantages in SERS [52]. It has been shown that even though gold generally has lower enhancement than silver, alloying pure silver with gold has distinct benefits in improving the chemical stability of SERS substrates [53]. This indicates that finding a good compromise in enhancement and chemical stability requires the tunability of the silver-to-gold ratio in the samples. By exploiting the inherent potential of spark ablation in producing alloy NPs, we fabricated different Au/Ag NP-based nanostructures with varying compositions. Since the spectral distribution of the enhancement of the produced nanostructures varies with the properties of the NPs building up the structures (such as elemental composition, particle size, shape, density, and surface geometry), the SERS performance of the NP films was tested at three different excitation laser wavelengths in the visible range. To understand the factors affecting the enhancement of the produced nanostructures, we present and discuss the effect of average composition, optical properties, excitation wavelength, and surface morphology on the SERS performance of the samples.

## 2. Materials and Methods

### 2.1. Production of Nanostructures

The experimental setup used for the fabrication of NP films is illustrated in Figure 1. For the generation of the NPs, a spark discharge generator (SDG) was used, which is described in detail elsewhere [30], and thus only a brief overview of the key elements is presented below.

The NP generation takes place in a stainless-steel chamber that is sealed with two KF-160 ports on the sides and is equipped with four radially aligned KF-40 ports. This chamber houses the horizontally positioned and axially aligned electrodes, the gap between which was set to 2 mm during particle generation. Gold (99.9% purity, Goodfellow Cambridge Ltd., Cambridge, UK), silver (99.9% purity, Goodfellow Cambridge Ltd., Cambridge, UK), and alloyed gold-silver (50/50 wt.%, 99.95% purity, ChemPUR GmbH, Karlsruhe, Germany) electrodes with a diameter of 3 mm were used to achieve different NP compositions. The different electrode configurations used for achieving different compositions are detailed in Table 1. A constant 5 slm flow rate of argon gas (99.996% purity, Messer Hungarogáz Ltd., Budapest, Hungary) was maintained with a mass flow controller (Model GFC16, Aalborg Inc., New York, NY, USA) and used as a carrier gas. The gas entered the chamber from below through one of the KF-40 ports, through an upward-pointing nozzle with an inner diameter of 2.85 mm.

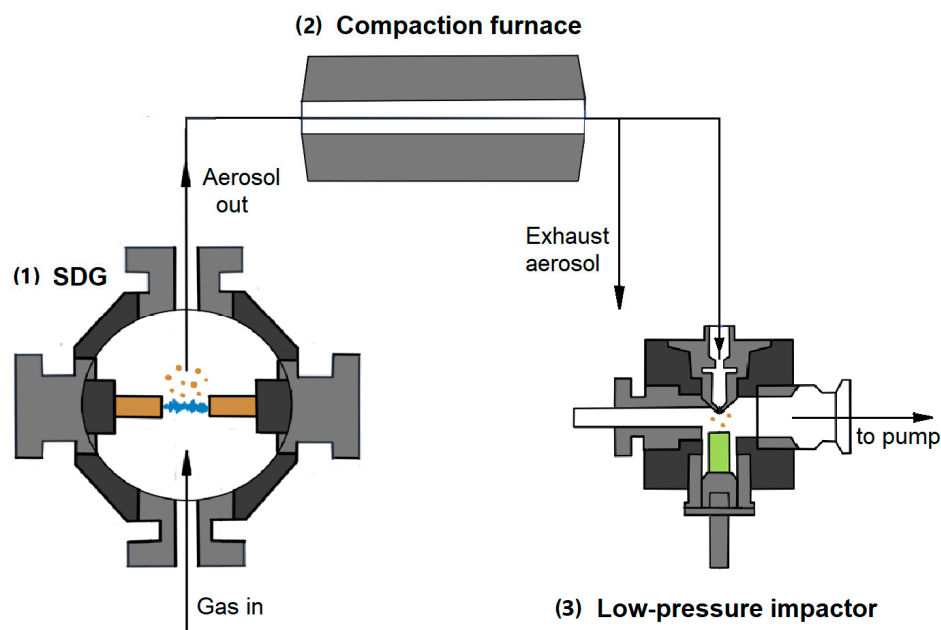


**Figure 1.** Schematic illustration of the experimental setup: the SDG chamber, in which the NP generation takes place (1), the tube furnace (2), and the impactor (3) used for depositing the NPs on the substrate (its placement marked with color). The arrows indicate the flow of the carrier gas and the aerosol.

**Table 1.** The electrode configurations and deposition times were used for the fabrication of each sample.

Sample	Electrode Configuration (Anode-Cathode)	Deposition Time (min)
S1	Au-Au	10
S2	Au-Ag	16
S3	AuAg-AuAg	22
S4	Ag-AuAg	27
S5	AgAg	35

Sparking was maintained by periodically charging and discharging a monolithic, high-voltage capacitor of 8 nF (Model 450PM980, General Atomics, San Diego, CA, USA) connected to a high-voltage power supply (Model HCK 800–12500, FuG GmbH, Schechen, Germany). Upon reaching the breakdown voltage characteristic of the setup, a spark discharge is created between the electrodes, resulting in a bipolar, damped, oscillatory discharge. The spark repetition rate was controlled by changing the charging current of the capacitor and set to 100 Hz. The electric signal was monitored using a voltage (P6015A, Tektronix Inc., Beaverton, OR, USA) and current probe (110, Pearson Electronics Inc., Palo Alto, CA, USA) and a 200 MHz oscilloscope (Model DSOX2024A, Keysight Technologies Inc., Santa Rosa, CA, USA).

The aerosol containing the generated NPs left the chamber through the upper KF-40 port and was led through a tube furnace heated to 800 °C (EHA 12/300B, Carbolite Gero GmbH, Neuhausen, Germany). The NPs were then deposited on quartz microscope coverslips via a low-pressure inertial impactor. The coverslips (Ted Pella Inc. 26016, Redding, CA, USA) were ultrasonically cleaned (Ultrasonic 300, NEY, now Blackstone-NEY Ultrasonics, Jamestown, NY, USA) in acetone (VWR Chemicals, Radnor, PA, USA, 20066.296), followed by ultrasonic cleaning in propanol (VWR Chemicals, 20842.312). Aerosols produced from different electrode materials in SDGs are characterized by different NP concentrations. This means that at a fixed sampling rate, the number of deposited particles would vary with the composition of the given sample, potentially affecting the

comparison of the characteristics of the samples. To account for the difference in the total NP concentration of the aerosol for the different compositions, different deposition times were used for each substrate. They were chosen so that on each substrate the same number of NPs were deposited of the chosen material as pure gold NPs under 10 min of deposition. The deposition times, along with the electrode configurations for each type of substrate are summarized in Table 1. These values were based on the measurement of the total concentration of the nanoparticles of different compositions by a condensation particle counter (CPC, Ultrafine Condensation Particle Counter 3756, TSI Inc., Shoreview, MN, USA).

## 2.2. Characterization of Nanostructures

The morphological parameters of the nanostructures were examined using a scanning electron microscope (SEM) and an atomic force microscope (AFM), and the composition of the particles was determined by inductively coupled plasma mass spectrometry, following the exact protocol described in [10]. The composition analysis of the deposited nanostructures was carried out by using energy-dispersive X-ray (EDX) spectrometry, and their optical characteristics were defined using a spectrophotometer. It should be noted that the characteristics of the samples derived from various measurements presented in this section always refer to the whole NP film, i.e., to the deposited nanostructure, and not to the individual NP agglomerates building up the films.

SEM images were recorded with a JOEL JIM-4700 FIB instrument. The recordings were made at 2 kV accelerating voltage at 35,000x magnification. We recorded SEM images of a structure at several points. An atomic force microscope was used for further morphological studies. AFM measurements were recorded with an AIST-NT Smart SPM AFM Microscope. A  $10 \times 10 \mu\text{m}^2$  area was scanned on each sample at five different points. From these AFM images, the average surface roughness of the measured regions was determined for each sample. Here, we define the average surface roughness (Ra) as the arithmetic average of the absolute value of the deviations in the profile height from the mean value, within an evaluation length:  $Ra = \frac{1}{L} \int_0^L |Z(x)| dx$ , where  $L$  is the evaluation length and  $Z(x)$  is the profile height function. The electron microscope also provided the opportunity for electron beam microanalysis, so EDX measurements were carried out to determine the average composition of the nanostructures. A Shimadzu UV-3600 spectrophotometer was used to measure the optical transmittance of the investigated nanostructures.

## 2.3. SERS Measurements

For the SERS measurements, a 1  $\mu\text{M}$  ethanolic solution of Rhodamine 6G (R6G) was used as a probe analyte in all cases. Before the measurements, 50  $\mu\text{L}$  of the solution was dropped onto the nanostructures and dried in air. The Raman measurements were performed with a Horiba Labram Raman-AFM microscope. During the measurements, lasers with three different wavelengths were used: 473 nm, 532 nm, and 633 nm. In all cases, the laser beam was focused on the surface of the nanostructure with a 50 $\times$  magnification objective. Table 2 summarizes the measurement parameters set during the measurements.

**Table 2.** Measurement parameters.

Excitation Wavelength	473 nm	532 nm	633 nm
Neutral density filter, %	0.1	0.01	3.2
Laser intensity, mW	0.03	0.01	0.22
Measurement time, s	1	15	15
Number of accumulations	1	3	1

The Raman spectrum of the analyte was measured at five different points on each sample. The obtained spectra were averaged in all cases. During the measurements, a reference spectrum was also recorded, during which the R6G analyte solution was applied to a glass slide at a higher concentration (10 mM) and then measured under the same

measurement conditions. The characteristic spectrum of R6G was observed both on the glass substrate and using metal nanoparticles. Based on these, the SERS enhancement factor (EF) was calculated from the intensity of the  $\sim 1650\text{ cm}^{-1}$  line, which corresponds to the vibrations of the C-C bond of the aromatic ring [54]. Figure 2 shows the  $\sim 1650\text{ cm}^{-1}$  peak appearing on the recorded spectra with the use of an excitation source with a wavelength of 532 nm, measured on the nanostructures (S1-S5, SERS condition) and a glass slide (Ref, non-SERS condition).

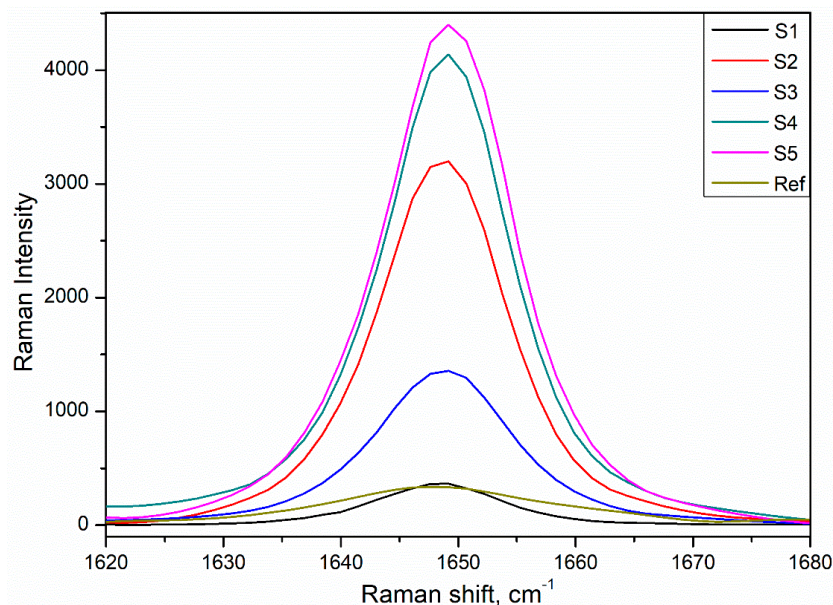


**Figure 2.** Raman spectra of Rhodamine 6G peak at  $\sim 1650\text{ cm}^{-1}$  measured on nanostructures and a pure glass substrate.

In this work, the SERS enhancement factor (EF) was calculated using the following formula [55]:

$$EF = \frac{I_{SERS}/N_{SERS}}{I_{NR}/N_{NR}} \quad (1)$$

In this approach,  $I_{SERS}$  is the intensity of the SERS signal measured on the nanostructures, while  $I_{NR}$  is the intensity of the Raman signal measured under non-SERS conditions (reference sample). Furthermore,  $N_{SERS}$  is the average number of molecules absorbed on the nanostructures in the scattering volume during SERS measurements, while  $N_{NR}$  is the average number of molecules in the scattering volume during Raman (non-SERS) measurements. In the present case, we assume that the ratio of the excited molecules under non-SERS and SERS conditions (i.e.,  $\frac{N_{NR}}{N_{SERS}}$ ) is equal to the ratio of the concentration of the analytes (i.e.,  $\frac{10\text{ mM}}{1\text{ }\mu\text{M}}$ ).

To investigate the spatial distribution of the enhancement of the samples, enhancement maps were constructed by measuring the Raman spectrum of the samples over a selected area. The spectral acquisition was carried out in a  $100 \times 100\text{ }\mu\text{m}^2$  area with a resolution of  $10\text{ }\mu\text{m}$ , resulting in a total of 100 measurement points. The measurement parameters were the same as shown in Table 2. Data processing and visualization were carried out by using the OriginPro 8.6 software.

### 3. Results and Discussion

#### 3.1. Morphology and Composition

As mentioned before, we generated Au, Ag, and Au/Ag nanoparticles with different compositions, as summarized in Table 3, to fabricate various nanostructures on a solid substrate. The surface layers obtained after depositing the different particles are referred to as S1–S5, indicating an increasing nominal silver content.

**Table 3.** Surface roughness (Ra), and composition values of the substrates.

Sample	Nanoparticle Composition (wt%Ag)	Layer Composition (wt%Ag)	Surface Roughness-Ra (nm)
S1	0	0	89 ± 4
S2	23.1 ± 1.0	25.1 ± 5.0	78 ± 3
S3	44.6 ± 5.0	44.7 ± 3.0	121 ± 13
S4	67.5 ± 4.4	50.1 ± 8.0	87 ± 8
S5	100	100	54 ± 1

We examined the morphology and composition of the produced structures using SEM, AFM, and EDX methods. The SEM and AFM images of the samples are presented in Figure 3 (left and right columns, respectively). It can be seen that the particles are more or less homogeneously distributed over the substrate, however, the porous nature of the layer is also evident. One can also note that the surface morphology of the samples varies with varying compositions. Using the AFM data, we determined the average surface roughness (Ra) of the different samples, which are summarized in Table 3. The relative standard deviation of the roughness is ca. 28%, mostly arising from the considerable deviation of S3 and S5 from the rest of the samples. It should be noted that we also determined the average composition of the fabricated nanostructures using EDX measurement and compared it with the average composition of the generated nanoparticles obtained from ICP-MS analysis. Considering the limitations of the two different techniques, the compositions are reasonably close to each other.

### 3.2. Optical Properties

The optical properties of the different samples were characterized by measuring their absorbance. Figure 4 shows the normalized absorbance spectra of S1-S5, which exhibit the blueshift of the absorbance peak position with increasing silver content. By comparing the experimental results with the values calculated (Calculations were made by using the MiePlot computer program, available at [www.philiplaven.com/mieplot.htm](http://www.philiplaven.com/mieplot.htm) (accessed on 3 March 2023)) for individual spherical nanoparticles in the relevant composition and size range, one can conclude that the measured values follow the theoretical trend reasonably well. However, the peak positions measured on the nanostructure layers are consistently larger than those of the individual nanoparticles, which indicates coupling between the particles forming the deposited layer [56,57]. Since aggregation of the particles is apparent in Figure 3, such deviation from the theoretical trend is expected.

### 3.3. SERS Measurements

The fabricated nanostructures were used as substrates for SERS measurements to assess their surface enhancement properties. Figure 5 shows the Raman spectrum of R6G recorded with different excitation laser wavelengths on the five different samples. The Raman spectrum of the analyte measured without nanostructure is shown for reference. As apparent from the spectra in Figure 5, both samples exhibit considerable enhancement. However, their exact value highly depends on the sample and the excitation wavelength.

To quantify the SERS activity of the different samples, the enhancement factor was calculated from the intensity of the peak at  $\sim 1650\text{ cm}^{-1}$ , marked in red in Figure 5, based on the formula given in Section 2. The EF values are listed in Table 4.

As can be seen in Table 4, the enhancement factor of the samples varies approximately in the  $10^3$ – $10^5$  range, depending on the properties of the nanostructure and the excitation wavelength. The highest enhancement (ca.  $2 \times 10^5$ ) can be achieved either by S5 with 473 nm or by S2 with 633 nm excitation wavelength.

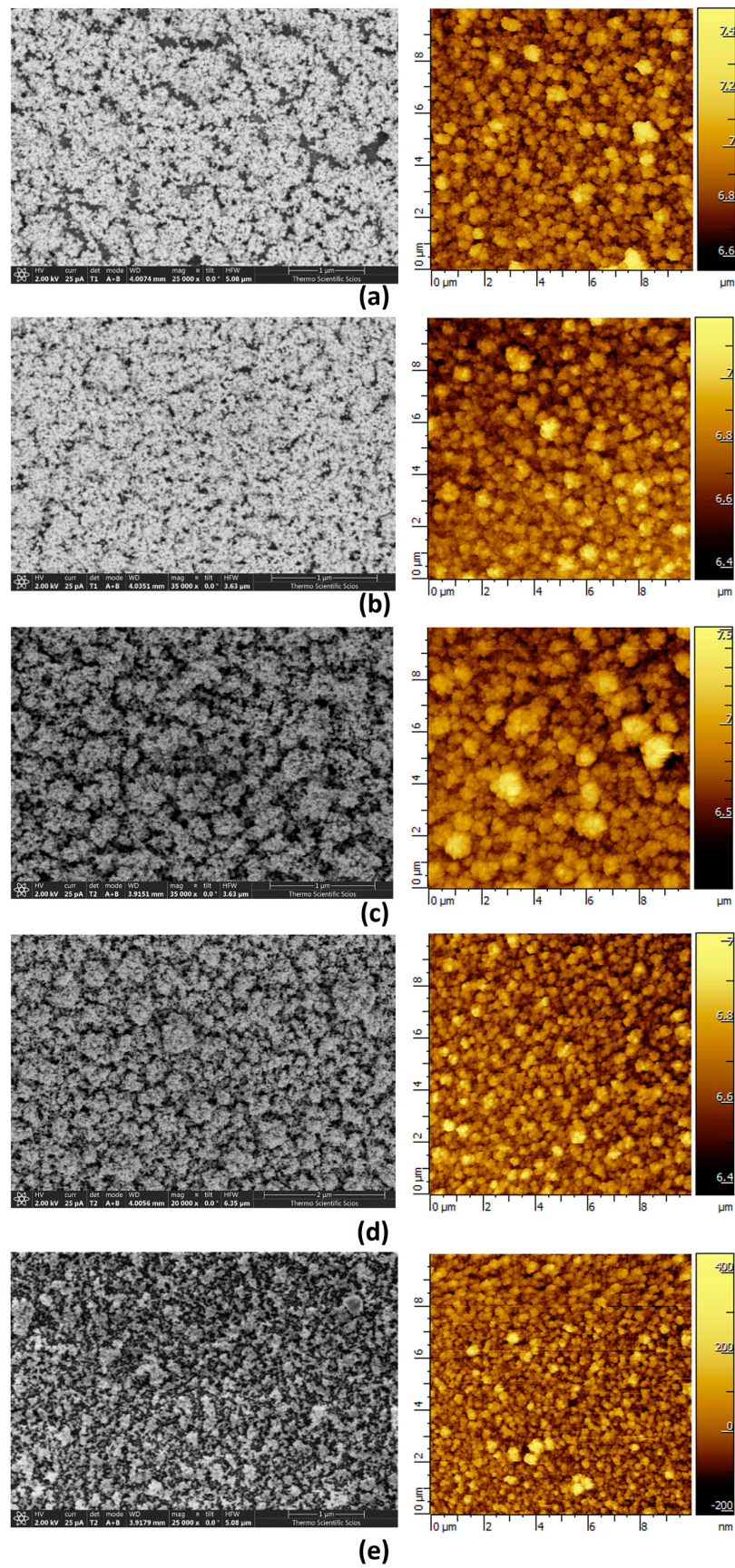
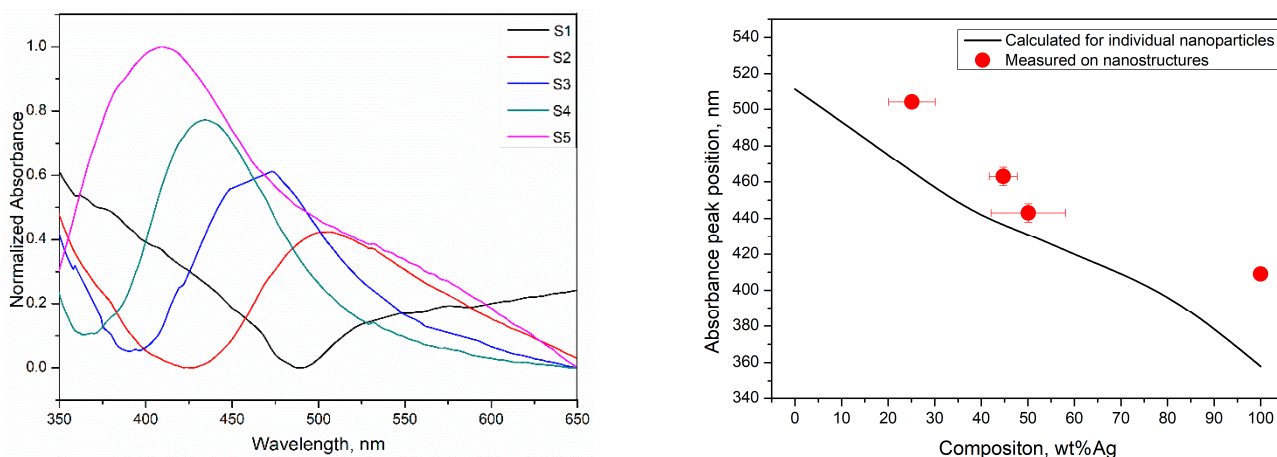
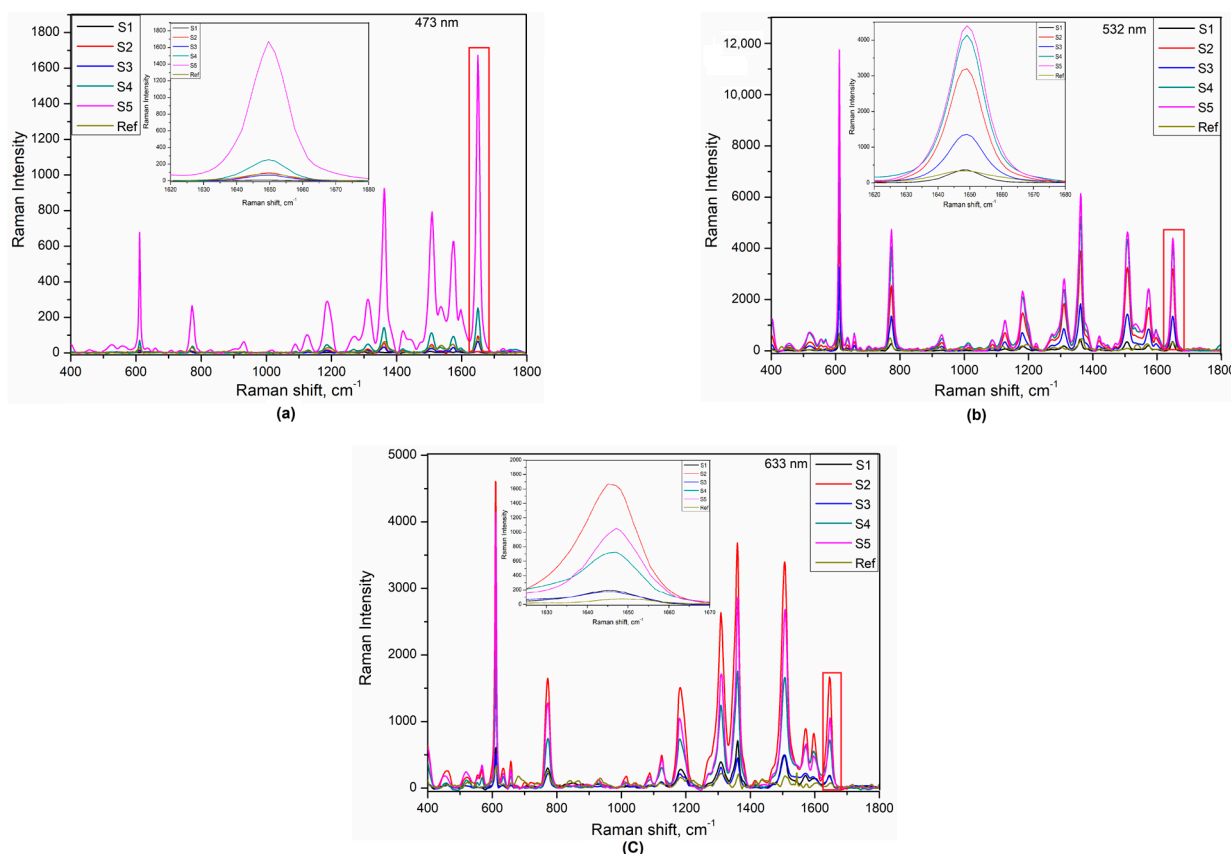


Figure 3. SEM (left column) and AFM (right column) images of S1 (a), S2 (b), S3 (c), S4 (d), and S5 (e).



**Figure 4.** Normalized absorbance spectra of the samples S1–S5 (left), variation of the absorbance peak position measured on the samples and calculated for individual nanoparticles as a function of composition (right).

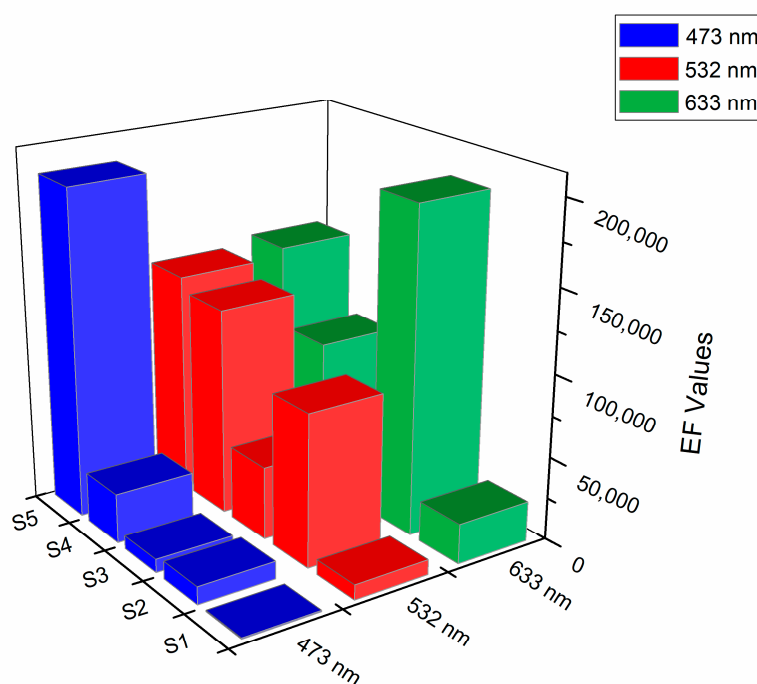


**Figure 5.** Raman spectrum of Rhodamine 6G measured on S1–S5 with three different excitation sources: 473 nm (a), 532 nm (b), and 633 nm (c). Please note the different vertical scales. The Raman spectrum of the analyte measured without nanostructure is included for reference.

**Table 4.** EF values of S1–S5 were calculated for the  $\sim 1650\text{ cm}^{-1}$  peak at different excitation wavelengths.

Excitation Wavelength	473 nm	532 nm	633 nm
S1	$819 \pm 112$	$8904 \pm 1326$	$24,153 \pm 2020$
S2	$10,759 \pm 696$	$91,847 \pm 5401$	$195,305 \pm 12,638$
S3	$8163 \pm 654$	$43,922 \pm 3964$	$24,421 \pm 3173$
S4	$30,130 \pm 2890$	$124,547 \pm 10,105$	$88,910 \pm 7116$
S5	$197,155 \pm 11,819$	$132,280 \pm 3311$	$137,275 \pm 28,584$

The data shown in Table 4 are visualized in Figure 6, to illustrate the effect of the wavelength of the excitation laser on the EF values for different samples. Considering that an increasing sample number means increasing Ag content in the sample, with S1 being pure gold while S5 is pure silver (please see Table 3), one can note that by decreasing the excitation wavelength, the samples with higher Ag content provide the higher enhancement. At the same time, at higher excitation wavelengths, the optimum Ag content decreases. Although the variation is not continuous (which will be discussed later in the text), this trend qualitatively agrees with the shift of the peak absorbance, which exhibits a blueshift with increasing silver content, indicating that the optimal excitation for maximum enhancement follows the absorbance peak of the sample. This readily means that by varying the composition, we can tune our substrates to provide optimal enhancement at the wavelength of the laser to be used for excitation. A practical aspect of such tunability arises from the fact that despite its high enhancement, the use of silver as a material for SERS is sometimes undesirable. This is due to the lower chemical stability of silver, which can be overcome by alloying with gold [53]. As evidenced by Table 4 and Figure 6, by carefully choosing the Au/Ag composition and the excitation wavelength, similar enhancements can be achieved to that of pure silver.

**Figure 6.** The EF values of the different substrates at different excitation wavelengths.

To further characterize the enhancement properties of the samples, we created enhancement maps of the five substrates, at their most favorable measurement parameters, i.e., at the optimal excitation wavelength (see Table 4). These maps allow for qualitatively

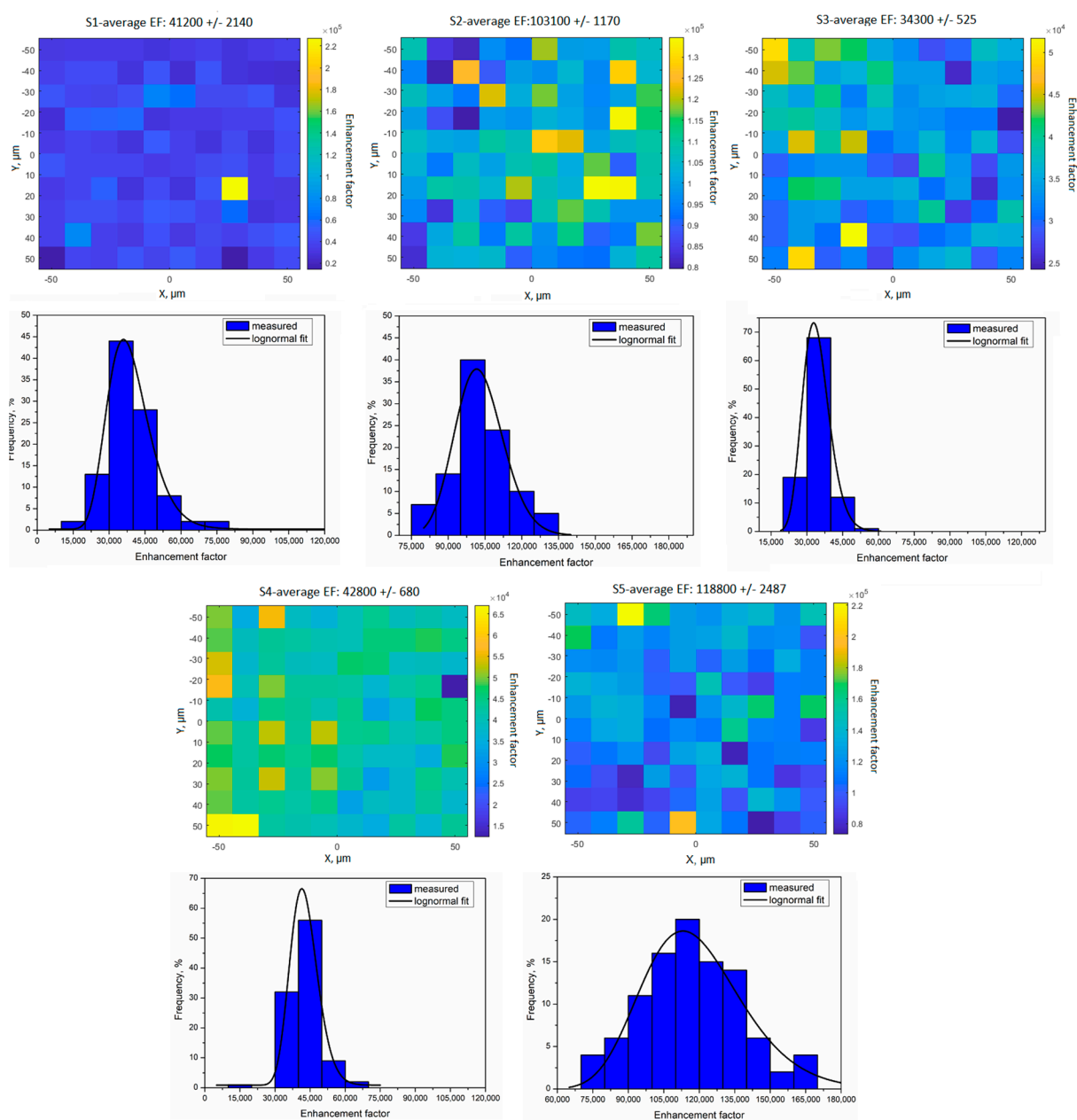
assessing the surface features of the nanostructures, i.e., detecting the presence of exceptionally high-enhancement hot spots or low-enhancement defects, as well as quantifying the distribution of the enhancement factor over a surface area, and calculating the standard deviation, a value which indicates well the homogeneity of the sample.

The enhancement maps of S1–S5 and the corresponding EF distributions are shown in Figure 7. It is clear from the maps and the distribution graphs that the variation of the enhancement approximately follows a log-normal distribution over the examined surface area. The average values and the standard deviation of the enhancement factor are summarized in Table 5. Relative standard deviation values are obtained in the 1–5% range, indicating that the surface enhancement of the substrates can be considered exceptionally uniform. However, it should be noted that the measured area of  $100 \times 100 \mu\text{m}^2$  characterizes only a small part of the active surface and by approaching the edge of the sample, where fewer and fewer nanoparticles are present, the observed distributions might change considerably. This is well reflected by the fact that enhancement factor values measured and averaged over the whole samples (having areas in the range of several  $\text{mm}^2$ ) somewhat differ from those obtained by mapping a smaller portion of each sample. Nevertheless, the relative standard deviations corresponding to the whole samples are still in the range of 3–21% (with an average of 9%), which indicates reasonably good uniformity.

The above results reflect the dependence of the Raman enhancement factor on the material properties of the applied nanostructure. In our case, this was achieved by generating nanoparticles with different compositions in the gas phase. However, as evidenced by the morphology analysis of the samples, the deposited layers fabricated from the generated particles exhibit differences. One variable which can be used as an indicator of certain surface morphology-related differences is roughness (cf. Table 3, Figure 3), which is also known to affect the enhancement of a surface [58]. With fixed NP size, shape, and density, the average composition of an NP film has the greatest relevance to its overall applicability in various potential SERS-based applications (see e.g., the question of chemical stability and biocompatibility). Nevertheless, from a practical point of view, it is worth assessing the potential contribution of surface morphology to the overall enhancement effect, arising from the impaction-based deposition method. If we assume that in the present composition and roughness ranges the material dependence is higher than that of the roughness-dependence, the latter can be investigated by comparing the enhancement factor values obtained at optimal excitation wavelength—shown in Table 4—with the roughness of the corresponding sample. Such a comparison is shown in Figure 8, where the average enhancement of a mapped area is shown as a function of the average surface roughness. Based on this graph, it can be said that the lower the surface roughness of the substrate, the greater the enhancement. So, if we omit the material property factor arising from the different compositions by always using the optimal excitation, then EF is roughly negatively correlated with the roughness. A similar tendency has been observed for gold nanoislands exposed to increasing annealing temperatures [59]. This effect is particularly pronounced below a roughness of ca. 80–90 nm, above which the enhancement factor seems to be fairly constant.

**Table 5.** Average enhancement factor and the (relative) standard deviation derived from enhancement maps of S1–S5.

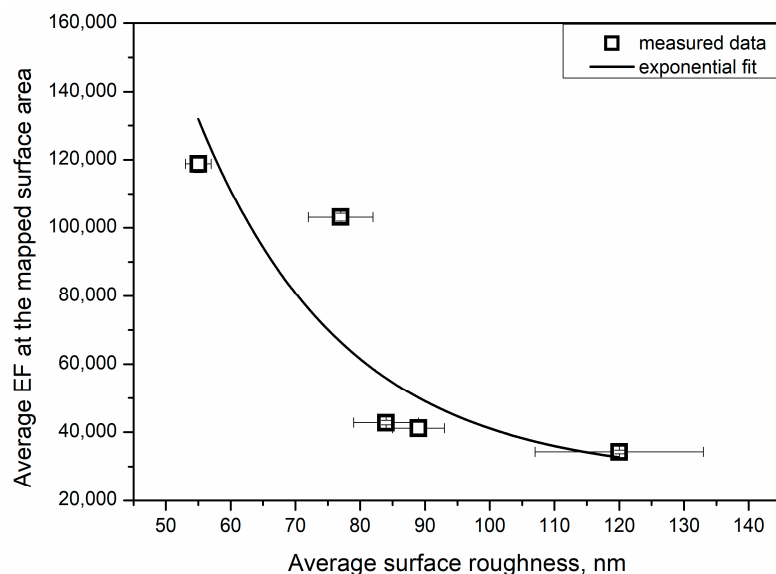
	S1	S2	S3	S4	S5
Average EF	41,200	103,100	34,300	42,800	118,800
Standard deviation	2140	1170	525	680	2487
Relative standard deviation	5.2%	1.1%	1.5%	1.6%	2.1%



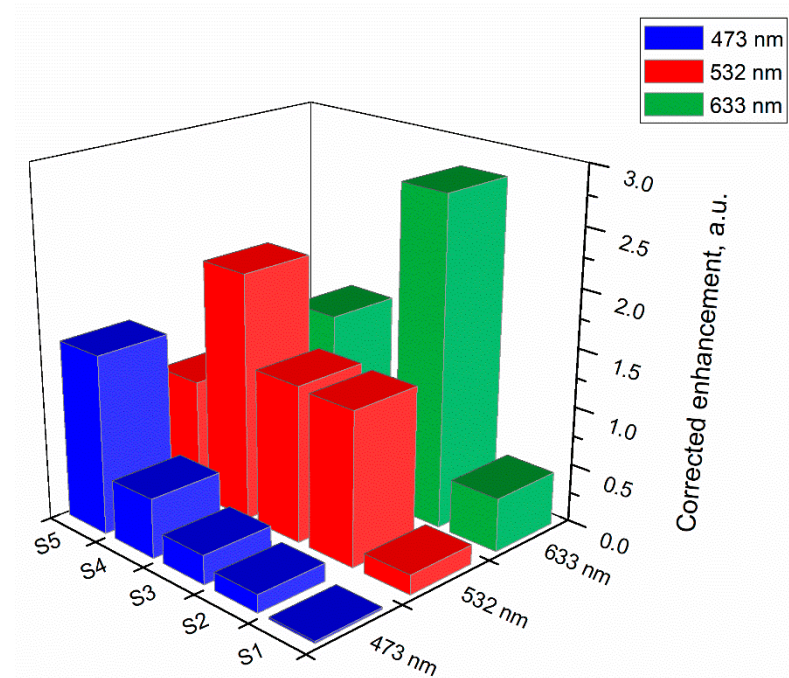
**Figure 7.** Enhancement maps and the corresponding distributions.

Figure 8 suggests that the different roughness of the samples contributes to the different enhancement values obtained with the three excitation wavelengths, summarized in Table 4. By using the exponential fit shown in Figure 8, we can attempt to correct for the effect of roughness, to reveal the composition-dependence of the enhancement factor obtained for the different samples and excitation wavelengths. To this end, the data in Figure 6 were divided by the exponential function fit to the average enhancement values (see Figure 8) and the result shown in Figure 9 illustrates the variation of the enhancement as a function of the excitation wavelengths for the five different samples. Please note that the values on the vertical axis of Figure 9 are in arbitrary units due to the correction, hence only indicating the trend of the enhancement, but not its exact value. By comparing Figure 9 to Figure 6, one can note that enhancement follows a much smoother and continuous trend as a function of the sample number, i.e., the sample composition, and exhibits a clearer maximum. This maximum shifts towards the samples with lower Ag content, characterized by lower wavelength peak absorption, with increasing excitation wavelength.

Nevertheless, by comparing Figure 9 to Figure 8, one can note that the contribution of roughness to the enhancement is much lower than that of the composition of the samples (a factor of ca. 3 compared to 1–2 orders of magnitude, depending on the excitation wavelength, respectively).



**Figure 8.** Average EF factor of mapped surface areas as a function of roughness.



**Figure 9.** Variation of the enhancement for S1–S5 as a function of the excitation laser. Please note that the enhancement is given in arbitrary units.

#### 4. Conclusions

In the present work, we used the spark ablation technique to produce Au, Ag, and Au/Ag nanoparticle agglomerates and applied a low-pressure inertial impactor to deposit them onto quartz surfaces to fabricate NP films. The produced films were characterized in terms of their morphology, composition, and optical properties. The fabricated nanostructures were also applied in surface-enhanced Raman spectroscopy, by measuring the Raman

spectra of Rhodamine 6G as a probe molecule. The average composition of the fabricated nanostructures and the wavelength of the excitation laser were varied to characterize the enhancement properties of the nanostructures at different gold-to-silver ratios. It was found that the samples fabricated via the deposition of Au/Ag NPs of different compositions not only differ in their optical properties (i.e., their absorbance spectrum), but that there is a slight variation in the average surface roughness of the structures as well. Therefore, these factors could both contribute to the observed surface enhancement of the different samples. As an attempt to decouple the effect of the surface roughness from the material-related optical properties of the samples, spatially resolved Raman mapping of the substrates was carried out at different excitation wavelengths. From the resulting data, the contribution of surface roughness-related effects to the total enhancement was estimated and found to be ca. 2–30 times smaller than that of the effect of average composition depending on the excitation wavelength.

**Author Contributions:** Conceptualization, P.P., A.K. and I.C.; methodology, P.P., V.H., Z.K. and A.K.; software, P.P., V.H., L.J., Z.K. and A.K.; validation, P.P., V.H., Z.K. and A.K.; formal analysis, P.P., A.K., Z.K. and I.C.; investigation, P.P., V.H., L.J., Z.K., A.K. and I.C.; resources, A.K. and I.C.; data curation, P.P., Z.K. and A.K.; writing—original draft preparation, P.P., Z.K. and A.K.; writing—review and editing, P.P., V.H., L.J., Z.K., A.K. and I.C.; visualization, P.P., V.H., L.J., Z.K., A.K. and I.C.; supervision, P.P., V.H., L.J., Z.K., A.K. and I.C.; project administration, A.K.; funding acquisition, A.K. All authors have read and agreed to the published version of the manuscript.

**Funding:** This research was funded by [The New National Excellence Program of the Ministry for Culture and Innovation from the source of the National Research, Development and Innovation Fund] grant number [the ÚNKP-22-3-II-DE-53 and the ÚNKP-22-3-SZTE-410], by [New National Excellence Program of the Ministry of Human Capacities] grant number [ÚNKP-22-5-DE-407], by [János Bolyai Research Scholarship of the Hungarian Academy of Sciences] grant number [BO/348/20], by [National Research, Development, and Innovation Fund] grant number [PD\_21 OTKA funding scheme (PD 139077 project)], by [National Research, Development, and Innovation Fund] grant number [TKP2021-NVA-19].

**Institutional Review Board Statement:** Not applicable.

**Informed Consent Statement:** Not applicable.

**Data Availability Statement:** Data will be shared upon reasonable request.

**Acknowledgments:** Research leading to these results has received funding from the TKP2021-NVA-19 project. Petra Pál and Viktória Horváth are grateful for the support from the ÚNKP-22-3-II-DE-53 and the ÚNKP-22-3-SZTE-410 projects, respectively, of the New National Excellence Program of the Ministry for Culture and Innovation from the source of the National Research, Development and Innovation Fund. Istvan Csarnovics is grateful for the support of the János Bolyai Research Scholarship of the Hungarian Academy of Sciences (BO/348/20) and the support through the New National Excellence Program of the Ministry of Human Capacities (ÚNKP-22-5-DE-407). A. Kohut is grateful for the Ministry of Innovation and Technology of Hungary for the funding provided from the National Research, Development and Innovation Fund under the PD\_21 OTKA funding scheme (PD 139077 project).

**Conflicts of Interest:** The authors declare no conflict of interest.

## References

1. Thybo, S.; Jensen, S.; Johansen, J.; Johannessen, T.; Hansen, O.; Quaade, U.J. Flame Spray Deposition of Porous Catalysts on Surfaces and in Microsystems. *J. Catal.* **2004**, *223*, 271–277. [[CrossRef](#)]
2. Guo, S.; Zhang, S.; Sun, S. Tuning Nanoparticle Catalysis for the Oxygen Reduction Reaction. *Angew. Chem. Int. Ed.* **2013**, *52*, 8526–8544. [[CrossRef](#)] [[PubMed](#)]
3. Mädler, L.; Roessler, A.; Pratsinis, S.E.; Sahm, T.; Gurlo, A.; Barsan, N.; Weimar, U. Direct Formation of Highly Porous Gas-Sensing Films by in Situ Thermophoretic Deposition of Flame-Made Pt/SnO<sub>2</sub> Nanoparticles. *Sens. Actuators B Chem.* **2006**, *114*, 283–295. [[CrossRef](#)]
4. Isaac, N.A.; Ngene, P.; Westerwaal, R.J.; Gaury, J.; Dam, B.; Schmidt-Ott, A.; Biskos, G. Optical Hydrogen Sensing with Nanoparticulate Pd-Au Films Produced by Spark Ablation. *Sens. Actuators B Chem.* **2015**, *221*, 290–296. [[CrossRef](#)]

5. Awada, C.; Dab, C.; Grimaldi, M.G.; Alshoabi, A.; Ruffino, F. High Optical Enhancement in Au/Ag Alloys and Porous Au Using Surface-Enhanced Raman Spectroscopy Technique. *Sci. Rep.* **2021**, *11*, 4714. [[CrossRef](#)]
6. Lu, L.; Eychmüller, A.; Kobayashi, A.; Hirano, Y.; Yoshida, K.; Kikkawa, Y.; Tawa, K.; Ozaki, Y. Designed Fabrication of Ordered Porous Au/Ag Nanostructured Films for Surface-Enhanced Raman Scattering Substrates. *Langmuir* **2006**, *22*, 2605–2609. [[CrossRef](#)]
7. El-Aal, M.A.; Seto, T.; Kumita, M.; Abdelaziz, A.A.; Otani, Y. Synthesis of Silver Nanoparticles Film by Spark Discharge Deposition for Surface-Enhanced Raman Scattering. *Opt. Mater.* **2018**, *83*, 263–271. [[CrossRef](#)]
8. Swihart, M.T. Vapor-Phase Synthesis of Nanoparticles. *Curr. Opin. Colloid Interface Sci.* **2003**, *8*, 127–133. [[CrossRef](#)]
9. Kruijs, F.E.; Fissan, H.; Peled, A. Synthesis of Nanoparticles in the Gas Phase for Electronic, Optical and Magnetic Applications—A Review. *J. Aerosol Sci.* **1998**, *29*, 511–535. [[CrossRef](#)]
10. Kohut, A.; Kéri, A.; Horváth, V.; Kopniczky, J.; Ajtai, T.; Hopp, B.; Galbács, G.; Geretovszky, Z. Facile and Versatile Substrate Fabrication for Surface Enhanced Raman Spectroscopy Using Spark Discharge Generation of Au/Ag Nanoparticles. *Appl. Surf. Sci.* **2020**, *531*, 147268. [[CrossRef](#)]
11. Van Ginkel, H.J.; Vollebregt, S.; Schmidt-Ott, A.; Zhang, G.Q. Mass and Density Determination of Porous Nanoparticle Films Using a Quartz Crystal Microbalance. *Nanotechnology* **2022**, *33*, 485704. [[CrossRef](#)]
12. Ivanov, V.; Lizunova, A.; Rodionova, O.; Kostrov, A.; Korniyushin, D.; Aybush, A.; Golodyayeva, A.; Efimov, A.; Nadtochenko, V. Aerosol Dry Printing for SERS and Photoluminescence-Active Gold Nanostructures Preparation for Detection of Traces in Dye Mixtures. *Nanomaterials* **2022**, *12*, 448. [[CrossRef](#)]
13. Li, H.; Merkl, P.; Sommertune, J.; Thersleff, T.; Sotiriou, G.A.; Li, H.; Merkl, P.; Sotiriou, G.A.; Sommertune, J.; Thersleff, T. SERS Hotspot Engineering by Aerosol Self-Assembly of Plasmonic Ag Nanoaggregates with Tunable Interparticle Distance. *Adv. Sci.* **2022**, *9*, 2201133. [[CrossRef](#)]
14. Jung, W.; Jung, Y.H.; Pikhitsa, P.V.; Feng, J.; Yang, Y.; Kim, M.; Tsai, H.Y.; Tanaka, T.; Shin, J.; Kim, K.Y.; et al. Three-Dimensional Nanoprinting via Charged Aerosol Jets. *Nature* **2021**, *592*, 54–59. [[CrossRef](#)]
15. Isaac, N.A.; Schlag, L.; Katzer, S.; Nahrstedt, H.; Reiprich, J.; Pezoldt, J.; Stauden, T.; Jacobs, H.O. Combinatorial Gas Phase Electrodeposition for Fabrication of Three-Dimensional Multimodal Gas Sensor Array. *Mater. Today: Proc.* **2020**, *33*, 2451–2457. [[CrossRef](#)]
16. Spark Ablation: Building Blocks for Nanotechnology. Schmidt-Ott, A. (Ed.) Stanford Publishing: Redwood City, CA, USA, 2020; ISBN 9814800821.
17. Kohut, A.; Villy, L.P.; Kéri, A.; Béltéki, Á.; Megyeri, D.; Hopp, B.; Galbács, G.; Geretovszky, Z. Full Range Tuning of the Composition of Au/Ag Binary Nanoparticles by Spark Discharge Generation. *Sci. Rep.* **2021**, *11*, 5117. [[CrossRef](#)]
18. Kohut, A.; Villy, L.P.; Ajtai, T.; Geretovszky, Zs.; Galbács, G. The Effect of Circuit Resistance on the Particle Output of a Spark Discharge Nanoparticle Generator. *J. Aerosol Sci.* **2018**, *118*, 59–63. [[CrossRef](#)]
19. Feng, J.; Ramlawi, N.; Biskos, G.; Schmidt-Ott, A. Internally Mixed Nanoparticles from Oscillatory Spark Ablation between Electrodes of Different Materials. *Aerosol Sci. Technol.* **2018**, *52*, 505–514. [[CrossRef](#)]
20. Feng, J.; Huang, L.; Ludvigsson, L.; Messing, M.E.; Maisser, A.; Biskos, G.; Schmidt-Ott, A. General Approach to the Evolution of Singlet Nanoparticles from a Rapidly Quenched Point Source. *J. Phys. Chem. C* **2016**, *120*, 621–630. [[CrossRef](#)]
21. Tabrizi, N.S.; Ullmann, M.; Vons, V.A.; Lafont, U.; Schmidt-Ott, A. Generation of Nanoparticles by Spark Discharge. *J. Nanoparticle Res.* **2009**, *11*, 315–332. [[CrossRef](#)]
22. Mylnikov, D.; Efimov, A.; Ivanov, V. Measuring and Optimization of Energy Transfer to the Interelectrode Gaps during the Synthesis of Nanoparticles in a Spark Discharge. *Aerosol Sci. Technol.* **2019**, *53*, 1393–1403. [[CrossRef](#)]
23. Megyeri, D.; Kohut, A.; Geretovszky, Z. Effect of Flow Geometry on the Nanoparticle Output of a Spark Discharge Generator. *J. Aerosol Sci.* **2021**, *154*, 105758. [[CrossRef](#)]
24. Han, K.; Kim, W.; Yu, J.; Lee, J.; Lee, H.; Gyu Woo, C.; Choi, M. A Study of Pin-to-Plate Type Spark Discharge Generator for Producing Unagglomerated Nanoaerosols. *J. Aerosol Sci.* **2012**, *52*, 80–88. [[CrossRef](#)]
25. Chae, S.; Lee, D.; Kim, M.-C.; Kim, D.S.; Choi, M. Wire-in-Hole-Type Spark Discharge Generator for Long-Time Consistent Generation of Unagglomerated Nanoparticles. *Aerosol Sci. Technol.* **2015**, *49*, 463–471. [[CrossRef](#)]
26. Kohut, A.; Ludvigsson, L.; Meuller, B.O.; Deppert, K.; Messing, M.E.; Galbács, G.; Geretovszky, Zs. From Plasma to Nanoparticles: Optical and Particle Emission of a Spark Discharge Generator. *Nanotechnology* **2017**, *28*, 475603. [[CrossRef](#)]
27. Byeon, J.H.; Park, J.H.; Hwang, J. Spark Generation of Monometallic and Bimetallic Aerosol Nanoparticles. *J. Aerosol Sci.* **2008**, *39*, 888–896. [[CrossRef](#)]
28. Kala, S.; Theissmann, R.; Kruijs, F.E. Generation of AuGe Nanocomposites by Co-Sparking Technique and Their Photoluminescence Properties. *J. Nanoparticle Res.* **2013**, *15*, 1963. [[CrossRef](#)]
29. Snellman, M.; Eom, N.; Ek, M.; Messing, M.E.; Deppert, K. Continuous Gas-Phase Synthesis of Core-Shell Nanoparticles via Surface Segregation. *Nanoscale Adv.* **2021**, *3*, 3041–3052. [[CrossRef](#)]
30. Villy, L.P.; Kohut, A.; Kéri, A.; Béltéki, Á.; Radnóczy, G.; Fogarassy, Z.; Radnóczy, G.Z.; Galbács, G.; Geretovszky, Z. Continuous Spark Plasma Synthesis of Au/Co Binary Nanoparticles with Tunable Properties. *Sci. Rep.* **2022**, *12*, 18560. [[CrossRef](#)]
31. Hallberg, R.T.; Ludvigsson, L.; Preger, C.; Meuller, B.O.; Dick, K.A.; Messing, M.E. Hydrogen-Assisted Spark Discharge Generated Metal Nanoparticles to Prevent Oxide Formation. *Aerosol Sci. Technol.* **2018**, *52*, 347–358. [[CrossRef](#)]

32. Olszok, V.; Bierwirth, M.; Weber, A.P. Interaction of Reactive Gases with Platinum Aerosol Particles at Room Temperature: Effects on Morphology and Surface Properties. *Nanomaterials* **2021**, *11*, 2266. [[CrossRef](#)]
33. Kohut, A. Hydrogen-Assisted Spark Generation of Silver Nanoparticles: The Effect of Hydrogen Content on the Signal Intensity in Surface-Enhanced Raman Spectroscopy. *J. Aerosol Sci.* **2023**, *167*, 106090. [[CrossRef](#)]
34. Tabrizi, N.S.; Xu, Q.; Van Der Pers, N.M.; Lafont, U.; Schmidt-Ott, A. Synthesis of Mixed Metallic Nanoparticles by Spark Discharge. *J. Nanoparticle Res.* **2009**, *11*, 1209–1218. [[CrossRef](#)]
35. Muntean, A.; Wagner, M.; Meyer, J.; Seipenbusch, M. Generation of Copper, Nickel, and CuNi Alloy Nanoparticles by Spark Discharge. *J. Nanoparticle Res.* **2016**, *18*, 229. [[CrossRef](#)]
36. Feng, J.; Chen, D.; Pikhitsa, P.V.; Jung, Y.H.; Yang, J.; Choi, M. Unconventional Alloys Confined in Nanoparticles: Building Blocks for New Matter. *Matter* **2020**, *3*, 1646–1663. [[CrossRef](#)]
37. Preger, C.; Bulbucan, C.; Meuller, B.O.; Ludvigsson, L.; Kostanyan, A.; Muntwiler, M.; Deppert, K.; Westerstroö, R.; Messing, M.E. Controlled Oxidation and Self-Passivation of Bimetallic Magnetic FeCr and FeMn Aerosol Nanoparticles. *J. Phys. Chem. C* **2019**, *123*, 16083–16090. [[CrossRef](#)]
38. Bae, Y.; Pikhitsa, P.V.; Cho, H.; Choi, M. Multifurcation Assembly of Charged Aerosols and Its Application to 3D Structured Gas Sensors. *Adv. Mater.* **2017**, *29*, 1604159. [[CrossRef](#)]
39. Efimov, A.A.; Korniyushin, D.V.; Buchnev, A.I.; Kameneva, E.I.; Lizunova, A.A.; Arsenov, P.V.; Varfolomeev, A.E.; Pavzderin, N.B.; Nikonov, A.V.; Ivanov, V.V. Fabrication of Conductive and Gas-Sensing Microstructures Using Focused Deposition of Copper Nanoparticles Synthesized by Spark Discharge. *Appl. Sci.* **2021**, *11*, 5791. [[CrossRef](#)]
40. Isaac, N.A.; Reiprich, J.; Schlag, L.; Moreira, P.H.O.; Baloochi, M.; Raheja, V.A.; Hess, A.L.; Centeno, L.F.; Ecke, G.; Pezoldt, J.; et al. Three-Dimensional Platinum Nanoparticle-Based Bridges for Ammonia Gas Sensing. *Sci. Rep.* **2021**, *11*, 12551. [[CrossRef](#)]
41. Trachioti, M.G.; Tzianni, E.I.; Riman, D.; Jurmanova, J.; Prodromidis, M.I.; Hrbac, J. Extended Coverage of Screen-Printed Graphite Electrodes by Spark Discharge Produced Gold Nanoparticles with a 3D Positioning Device. Assessment of Sparking Voltage-Time Characteristics to Develop Sensors with Advanced Electrocatalytic Properties. *Electrochim. Acta* **2019**, *304*, 292–300. [[CrossRef](#)]
42. Vasiliev, A.A.; Varfolomeev, A.E.; Volkov, I.A.; Simonenko, N.P.; Arsenov, P.V.; Vlasov, I.S.; Ivanov, V.V.; Pislyakov, A.V.; Lagutin, A.S.; Jahatspanian, I.E.; et al. Reducing Humidity Response of Gas Sensors for Medical Applications: Use of Spark Discharge Synthesis of Metal Oxide Nanoparticles. *Sensors* **2018**, *18*, 2600. [[CrossRef](#)] [[PubMed](#)]
43. Volkov, I.A.; Simonenko, N.P.; Efimov, A.A.; Simonenko, T.L.; Vlasov, I.S.; Borisov, V.I.; Arsenov, P.V.; Lebedinskii, Y.Y.; Markeev, A.M.; Lizunova, A.A.; et al. Platinum Based Nanoparticles Produced by a Pulsed Spark Discharge as a Promising Material for Gas Sensors. *Appl. Sci.* **2021**, *11*, 526. [[CrossRef](#)]
44. Van Ginkel, H.J.; Orvietani, M.; Romijn, J.; Zhang, G.Q.; Vollebregt, S. ZnO Nanoparticle Printing for UV Sensor Fabrication. In Proceedings of the 2022 IEEE Sensors, Dallas, TX, USA, 30 October–2 November 2022. [[CrossRef](#)]
45. Becker, R.; Weber, K.; Pfeiffer, T.V.; Van Kranendonk, J.; Schouten, K.J. A Scalable High-Throughput Deposition and Screening Setup Relevant to Industrial Electrocatalysis. *Catalysts* **2020**, *10*, 1165. [[CrossRef](#)]
46. Valenti, M.; Dolat, D.; Biskos, G.; Schmidt-Ott, A.; Smith, W.A. Enhancement of the Photoelectrochemical Performance of CuWO<sub>4</sub> Thin Films for Solar Water Splitting by Plasmonic Nanoparticle Functionalization. *J. Phys. Chem. C* **2015**, *119*, 2096–2104. [[CrossRef](#)]
47. El-Aal, M.A.; Seto, T. Spark Discharge Deposition of Au/Cu Nanoparticles for Surface-Enhanced Raman Scattering. *Surf. Interface Anal.* **2021**, *53*, 824–828. [[CrossRef](#)]
48. El-Aal, M.A.; Seto, T.; Atsushi, M. The Effects of Operating Parameters on the Morphology, and the SERS of Cu NPs Prepared by Spark Discharge Deposition. *Appl. Phys. A* **2020**, *126*, 572. [[CrossRef](#)]
49. Lee, H.; You, S.; Pikhitsa, P.V.; Kim, J.; Kwon, S.; Woo, C.G.; Choi, M. Three-Dimensional Assembly of Nanoparticles from Charged Aerosols. *Nano Lett.* **2011**, *11*, 119–124. [[CrossRef](#)]
50. Kohut, A.; Horváth, V.; Pápa, Z.; Vajda, B.; Kopniczky, J.; Galbács, G.; Geretovszky, Z. One-Step Fabrication of Fiber Optic SERS Sensors via Spark Ablation. *Nanotechnology* **2021**, *32*, 395501. [[CrossRef](#)]
51. Arsenov, P.V.; Efimov, A.A.; Ivanov, V.V. Optimizing Aerosol Jet Printing Process of Platinum Ink for High-Resolution Conductive Microstructures on Ceramic and Polymer Substrates. *Polymers* **2021**, *13*, 918. [[CrossRef](#)]
52. Pilot, R.; Signorini, R.; Durante, C.; Orian, L.; Bhamidipati, M.; Fabris, L. A Review on Surface-Enhanced Raman Scattering. *Biosensors* **2019**, *9*, 57. [[CrossRef](#)]
53. Fan, M.; Lai, F.J.; Chou, H.L.; Lu, W.T.; Hwang, B.J.; Brolo, A.G. Surface-Enhanced Raman Scattering (SERS) from Au:Ag Bimetallic Nanoparticles: The Effect of the Molecular Probe. *Chem. Sci.* **2013**, *4*, 509–515. [[CrossRef](#)]
54. Wu, C.; Chen, E.; Wei, J. Surface Enhanced Raman Spectroscopy of Rhodamine 6G on Agglomerates of Different-Sized Silver Truncated Nanotriangles. *Colloids Surf. A: Physicochem. Eng. Asp.* **2016**, *506*, 450–456. [[CrossRef](#)]
55. Lee, H.K.; Lee, Y.H.; Koh, C.S.L.; Phan-Quang, G.C.; Han, X.; Lay, C.L.; Sim, H.Y.F.; Kao, Y.C.; An, Q.; Ling, X.Y. Designing Surface-Enhanced Raman Scattering (SERS) Platforms beyond Hotspot Engineering: Emerging Opportunities in Analyte Manipulations and Hybrid Materials. *Chem. Soc. Rev.* **2019**, *48*, 731–756. [[CrossRef](#)]
56. Zhu, J.; Sun, Z.; Li, J.J.; Zhao, J.W. Bovine Serum Albumins (BSA) Induced Aggregation and Separation of Gold Colloid Nanoparticles. *J. Nanosci. Nanotechnol.* **2012**, *12*, 2206–2211. [[CrossRef](#)]
57. Pápa, Z.; Kasza, J.; Budai, J.; Márton, Z.; Molnár, G.; Dombi, P. Tuning Plasmonic Field Enhancement and Transients by Far-Field Coupling between Nanostructures. *Appl. Phys. Lett.* **2020**, *117*, 081105. [[CrossRef](#)]

58. Macias, G.; Alba, M.; Marsal, L.F.; Mihi, A. Surface Roughness Boosts the SERS Performance of Imprinted Plasmonic Architectures. *J. Mater. Chem. C* **2016**, *4*, 3970–3975. [[CrossRef](#)]
59. Fang, S.U.; Hsu, C.L.; Hsu, T.C.; Juang, M.Y.; Liu, Y.C. Surface Roughness-Correlated SERS Effect on Au Island-Deposited Substrate. *J. Electroanal. Chem.* **2015**, *741*, 127–133. [[CrossRef](#)]

**Disclaimer/Publisher’s Note:** The statements, opinions and data contained in all publications are solely those of the individual author(s) and contributor(s) and not of MDPI and/or the editor(s). MDPI and/or the editor(s) disclaim responsibility for any injury to people or property resulting from any ideas, methods, instructions or products referred to in the content.